JGR Space Physics

RESEARCH ARTICLE
10.1029/2019JA026703

Key Points:
- A pronounced equatorial height anomaly (EHA) is observed during the main phase of St. Patrick's Day storm
- Local time appearance of EHA on the storm day is much earlier (nearly 2 hr) than the quiet time
- TIEGCM simulations revealed that the storm time enhancement of zonal electric field is responsible for the pronounced EHA

Correspondence to:
V. Sai Gowtam,
gowtham.physics12@gmail.com

Citation:
Sai Gowtam, V., Lei, J., Tulasi Ram, S., Luan, X., Ren, D., & Zhong, J. (2019). Variation of the equatorial height anomaly during the main phase of 2015 St. Patrick's Day geomagnetic storm using ANNIM and TIEGCM. *Journal of Geophysical Research: Space Physics*, *124*. https://doi.org/10.1029/2019JA026703

Received 7 MAR 2019
Accepted 17 JUL 2019
Accepted article online 31 JUL 2019

Variation of the Equatorial Height Anomaly During the Main Phase of 2015 St. Patrick's Day Geomagnetic Storm Using ANNIM and TIEGCM

V. Sai Gowtam[1], Jiuhou Lei[2], S. Tulasi Ram[1], Xiaoli Luan[2], Dexin Ren[2], and Jiahao Zhong[2]

[1]Indian Institute of Geomagnetism, Navi Mumbai, India, [2]CAS Key Laboratory of Geospace Environment, School of Earth and Space Sciences, University of Science and Technology of China, Hefei, China

Abstract A double-peak structure in the peak height of ionospheric *F*2 layer around ±10° geomagnetic latitudes similar to the equatorial ionization anomaly was recently reported. This unique feature was referred as the equatorial height anomaly (EHA). In the present paper, a simulation study is carried out using the data-driven artificial neural network-based two-dimensional ionospheric model (ANNIM-2D) and the physics-based thermosphere-ionosphere-electrodynamics general circulation model (TIEGCM) to understand the local time and latitudinal variation of EHA during the main phase of St. Patrick's Day geomagnetic storm. Both the ANNIM-2D and TIEGCM consistently show pronounced EHA during the main phase of the geomagnetic storm. Further, the local time of EHA development on the storm day is much earlier (nearly 2 hr) than the quiet time over Brazilian sector (90°W). The TIEGCM simulation revealed that the storm time enhancement of the equatorial fountain associated with the enhanced equatorial zonal electric field is the main controlling factor for the pronounced EHA during the main phase. The storm time meridional neutral winds positively contribute to the development of EHA. This study revealed the direct manifestation of the storm time-enhanced plasma fountain on the EHA.

1. Introduction

The F_2-layer peak electron density (N_mF_2) and the peak height (h_mF_2) are the two key parameters to describe the ionosphere and its vertical electron density distribution. At higher altitudes, diffusion is the leading physical process, whereas the loss mechanism is more dominant process at the lower *F* region altitudes. Therefore, the ionospheric density peak is formed at an altitude where the transport due to diffusion and the loss process of O^+ balance each other (Rishbeth & Garriott, 1969). With various anomalies, the spatial and temporal variation of N_mF_2 is different compared to the electron density distribution in *E* and F_1 layers of the ionosphere. Those are equatorial ionization anomaly (EIA; Appleton, 1946; Balan et al., 2017), winter anomaly (Burns et al., 2014, 2015; Pavlov & Pavlova, 2009; Rishbeth & Setty, 1961; Sai Gowtam & Tulasi Ram, 2017c; Torr & Torr, 1973; Yonezawa & Arima, 1959), semiannual anomaly (Azpilicueta & Brunini, 2011; Balan et al., 2000; Ma et al., 2003; Millward et al., 1996; Volland, 1969), annual anomaly (Berkner & Wells, 1938; Dang et al., 2017; Mendillo et al., 2005; Rishbeth & Muller-Wodarg, 2006; Sai Gowtam & Tulasi Ram, 2017b; Yonezawa, 1971; Zeng et al., 2008), and the Weddell Sea anomaly (Bellchambers & Piggott, 1958; Burns et al., 2008; Chen et al., 2011; Dudeney & Piggott, 1978; He et al., 2009; Jee et al., 2009; Lin et al., 2009; Liu et al., 2010; Penndorf, 1965). The equatorial zonal electric field along with the horizontal magnetic field lines at the geomagnetic equator creates the so-called "equatorial plasma fountain (EPF)" resulting in the formation of the EIA (Balan & Bailey, 1995; Bramley & Peart, 1965; Chen et al., 2016; Lu et al., 2012; Moffett & Hanson, 1965). The spatial and temporal variability of the EIA under quiet and disturbed space weather conditions and the responsible physical mechanisms were widely studied in the past. An excellent review on the EIA and EPF can be found in the recent work of Balan et al. (2017). The vertical and field-aligned plasma transport processes due to the zonal electric field and thermospheric neutral winds chiefly control the variability of these anomalies. Further, the disturbed space weather conditions, such as geomagnetic storms, introduce perturbations in global wind circulations and the equatorial zonal electric fields, which can significantly modify the latitudinal and longitudinal distribution of N_mF_2 and h_mF_2 (Blanc & Richmond, 1980; Fujiwara et al., 1996;).

At the equatorial and low-latitude regions, the peak height of *F*2 layer is largely controlled by the ExB plasma drift and the magnitude and polarity of thermospheric neutral winds. Therefore, the study of h_mF_2 gives some insights into the background physical processes that are operating in the *F* region. The global distribution of h_mF_2 and its variability was studied in the past using global ionosonde/Digisonde observations, topside sounders, and the Global Positioning System (GPS)-Radio Occultation (RO) data (e.g., Gulyaeva et al., 2008; Hoque & Jakowski, 2012; Maruyama et al., 2014; Zhang et al., 2014). Using chain of ionosonde stations, Maruyama et al. (2014) studied the magnetic latitude variation of h_mF_2 around local noon and found constant peak value of h_mF_2 over the dip equator (equatorial ionospheric ceiling). However, the detailed latitudinal variability of h_mF_2, particularly, at the equatorial and low-latitude regions was less explored in the past. Recently, Luan et al. (2016) reported the double-crest structure in h_mF_2 around $\pm 10°$ geomagnetic latitudes, similar to the well-known EIA in N_mF_2. They have referred this unique phenomenon as equatorial height anomaly (EHA). This feature had not been reported earlier, probably, due to lack of latitudinally spaced h_mF_2 observations at sufficiently close intervals. With a constellation of six microsatellites, Formosa Satellite 3/Constellation Observing System for Meteorology, Ionosphere, and Climate (COSMIC) provided unprecedented spatial coverage of vertical electron density profiles all over the globe. By using the long-term data set of Formosa Satellite 3/COSMIC mission, Luan et al. (2016) have investigated the local time, longitude, seasonal, and the solar activity variations of EHA. They found that the EHA is more pronounced during the low solar activity of the March equinox and less obvious during the solstices. Further, they have concluded that the vertical ExB plasma drift is the main controlling factor for the formation of EHA and the thermospheric neutral winds may contribute to the enhancement in EHA (Luan et al., 2016).

The prompt penetration electric fields (PPEFs) associated with high-latitude convection during geomagnetic storms can enhance/reduce the equatorial and low-latitude electric fields via high-latitude-low-latitude coupling processes (Huang et al., 2005, 2007; Kikuchi et al., 2000, 2008; Kikuchi & Hashimoto, 2016; Nishida, 1968). In the present paper, we have explored the modulation of EHA during the main phase of St. Patrick's Day geomagnetic storm over Brazilian longitude sector by utilizing the artificial neural network-based two-dimensional ionospheric model (ANNIM-2D) and the thermosphere-ionosphere-electrodynamics general circulation model (TIEGCM). Further, a controlled simulation study is performed using the TIEGCM model to understand the responsible physical mechanisms for the enhanced EHA during the main phase of the storm.

2. Model Description and Methodology

Recently, a global ANNIM-2D was developed to predict N_mF_2 and h_mF_2 by implementing the machine learning technique (Sai Gowtam & Tulasi Ram, 2017a; Tulasi Ram et al., 2018). ANNIM-2D is essentially an empirical model developed by training the Artificial Neural Networks (ANNs) with long-term data of N_mF_2 and h_mF_2 from ground-based global Digisonde observations, and the GPS-RO missions. The training dataset consists of all the GNSS-RO data from 2006 to 2015 including the data of March 21, 2007, and the 2015 magnetic storm period. From the whole dataset, 70%, 15%, and 15% of data are randomly selected for training, validation, and testing of neural networks, respectively. The ANNs are trained with a set of input parameters, such as day of the year (DOY), universal time (UT), latitude, longitude, F10.7 solar flux, Kp-index, declination, inclination, dip latitude, zonal wind, and meridional wind to predict the N_mF_2 and h_mF_2. Further, it was shown by Sai Gowtam and Tulasi ram (2017a) and Tulasi Ram et al. (2018) that the ANNIM-2D-predicted N_mF2 and h_mF2 show excellent correlation with the independent ground-based Digisonde observations.

In this paper, we utilized the ANNIM-2D model to study the EHA during the main phase of St. Patrick's Day storm. To further examine the background physical mechanisms of EHA, we carried out controlled simulation study using National Center for Atmospheric Research-TIEGCM model. The National Center for Atmospheric Research-TIEGCM is a first principle model that solves continuity, momentum, and transport equations for neutral gases and ions to obtain a self-consistent solution in three-dimensional coordinates (Richmond et al., 1992). With a vertical resolution of one-fourth scale height, the high-resolution (2.5° longitude × 2.5° latitude) version of the TIEGCM consists of 58 pressure levels starting from ~97 km and extending up to 600 km depending upon the solar activity. The migrating and nonmigrating tides specified at the lower boundary using global-scale wave model. The basic setup of the model input parameters is the same as those in Ren and Lei (2017). In this study, we have used the Heelis convection filed model (Heelis et al.,

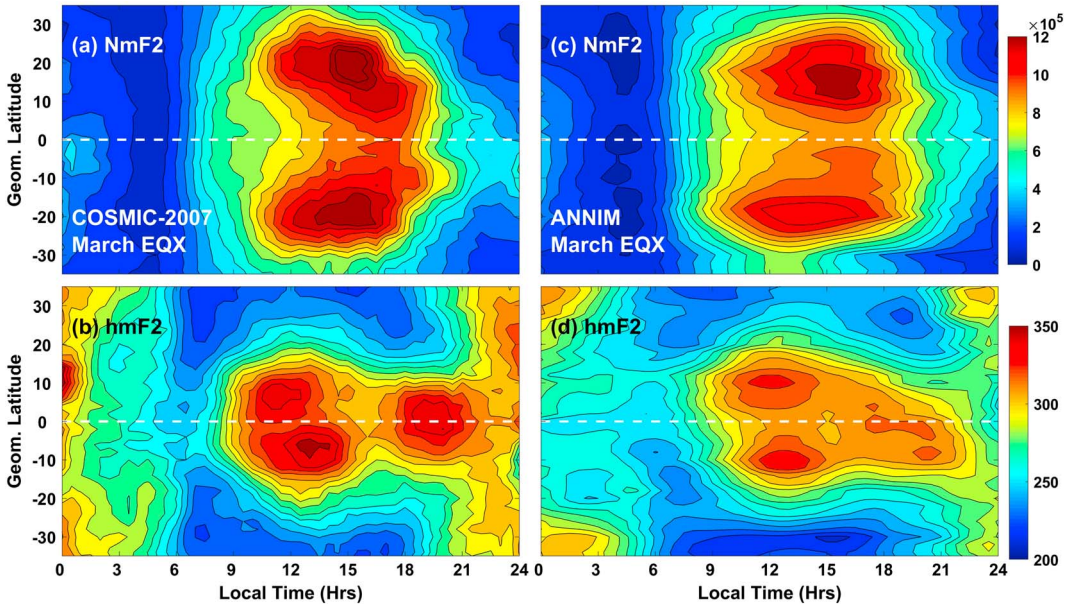

Figure 1. Local time and geomagnetic latitudinal variation of zonal mean (longitudinally averaged) N_mF_2 (a and c) and h_mF_2 (b and d) obtained from the Constellation Observing System for Meteorology, Ionosphere, and Climate (COSMIC) Radio Occultation observations (left panels) and artificial neural network-based ionospheric model (ANNIM; right panels), respectively, during March equinox. The horizontal dashed lines indicate the dip equator.

1982) to specify the high-latitude electric fields. The simulation results obtained by ANNIM and the TIEGCM during the St. Patrick's Day storm will be discussed in the subsequent sections.

As mentioned earlier, combining the large data set from GPS-RO missions gave a good spatiotemporal coverage. However, it is very difficult to get fine spatiotemporal resolution data in a given "single day," either by existing ground-based Digisonde/ionosonde network or satellite in situ/RO measurements. The lack of spatiotemporal coverage of data constrained us to relay on ANNIM-2D, as the model is based on the COSMIC data. It is clear that ANNIM-2D could reproduce the EHA phenomena, as the model was heavily waited on COSMIC data (Figure 1). Further, Tulasi Ram et al. (2018) reported that the ANNIM-2D has an excellent ability to predict the N_mF_2 and h_mF_2 under disturbed space weather conditions. Hence, the model results from ANNIM-2D are utilized in the present study to explore the equatorial and low-latitude variation of EHA during the main phase of St. Patrick's Day geomagnetic storm.

3. Results

The peak density and peak height of *F*2 layer (N_mF2 and h_mF2) from COSMIC-RO observations during the equinoctial months (February, March, and April) of low solar activity year 2007 are considered to study the EIA and EHA. The average F10.7 solar flux value during this period is ~75 sfu (1 sfu = 10^{-22} W·m^{-2}·Hz^{-1}). Figures 1a and 1b represent the local time and geomagnetic latitudinal variations of zonal mean (longitudinally averaged) N_mF_2 and h_mF_2 obtained from the COSMIC data. From Figure 1a, we can see a well-developed EIA around local noon to afternoon hours. Further, one can notice the double-peak structure of h_mF_2 around ±10° dip latitude (Figure 1b) during 10–15 LT similar to the EIA, which is known as EHA (Luan et al., 2016). The difference between peak and the trough is about ~14 and ~23 km for Northern and the Southern Hemispheres, respectively. The occurrence of maximum peak-to-trough difference is around 12–13 LT. After 15 LT, the double-peak structure is absent, and the peak value shifted toward the dip equator. An enhanced h_mF_2 around postsunset time is due to the prereversal enhancement of the zonal electric field.

Though the ANNIM is developed by using COSMIC data, it is important to test whether the model can capture the EHA phenomenon or not. To confirm this, we run the ANNIM model under similar solar activity conditions (F10.7 = 75 sfu) during March equinox (DOY = 80). Figures 1c and 1d show the local time and geomagnetic latitudinal variations of zonal mean N_mF_2 and h_mF_2 predicted by ANNIM under March

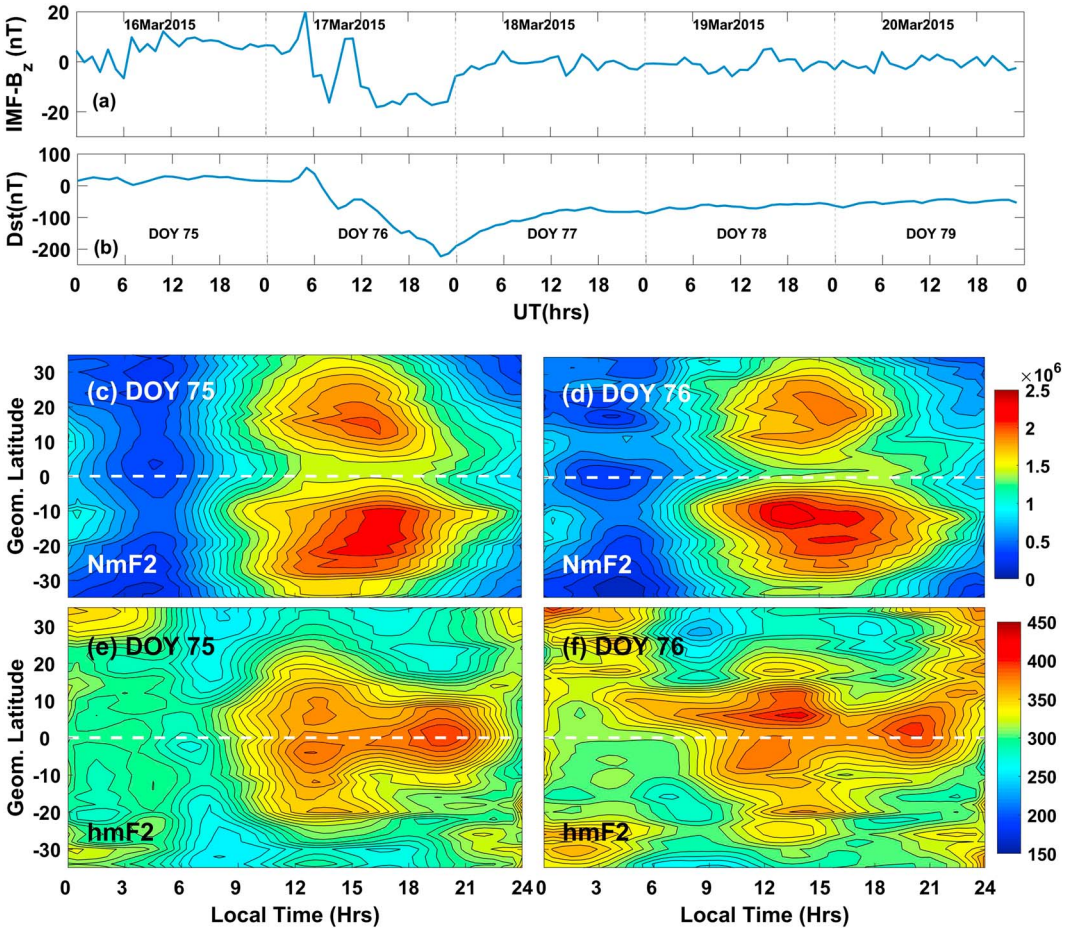

Figure 2. (a) IMF-B_z and (b) Dst index from Days 75 to 79 (16–20 March 2015). Local time and dip latitudinal variation of zonal mean N_mF_2 (c and d) and h_mF_2 (2 and f) during quiet (DOY 75; 16 March 2015) and disturbed (DOY 76; 17 March 2015) geomagnetic conditions as predicted by artificial neural network-based ionospheric model. The horizontal dashed lines represent the dip equator. DOY = day of the year.

equinox conditions. From Figure 1c, we can see the EIA around local noon to afternoon hours. Further, one can observe the EHA around ±10° dip latitude (Figure 1d) during 10–15 LT similar to Figure 1b. The difference between peak to trough is about ~17 and ~20 km for Northern and the Southern Hemispheres, respectively. Further, the local time and latitudinal variations of EHA produced by ANNIM-2D simulation (Figures 1c and 1d) are consistent with those obtained from the COSMIC observations (Figures 1a and 1b) and those reported by Luan et al. (2016).

Figures 2a and 2b show the variations of Z component of interplanetary magnetic field (IMF-B_z) and disturbed storm time (Dst) on 16–20 March 2015. A coronal mass ejection from the sunspot AR2297 hit the Earth's magnetosphere around 04:30 UT on 17 March 2015. The southward turning of the IMF-B_z around 06:00 UT causes the magnetic reconnection with the Earth's magnetic field. The Dst index reached its peak negative value about −228 nT at 23:04 UT, becoming the strongest geomagnetic storm in the solar cycle 24. The main phase of the storm lasted approximately 17 hr except for a brief recovery of Dst due to northward turning of IMF-B_z between 09:30 and 12:00 UT. Nevertheless, the IMF-B_z was steadily southward between ~12:30 and 23:00 UT on 17 March 2015. The main phase of the storm ceased around 23:04 UT, and the recovery of Dst-index was continued till 21 March 2015.

With a view to examine the local time and latitudinal variations of EHA during the St. Patrick's Day geomagnetic storm, we have run the ANNIM-2D model on day numbers from 75 to 77, in which the main phase of the storm occurred on Day 76 (17 March 2015). The same F10.7 solar flux and 3-hourly Kp-index values on day numbers from 75 to 77, (16–18 March 2015) are used as the ANNIM inputs to predict N_mF_2 and h_mF_2.

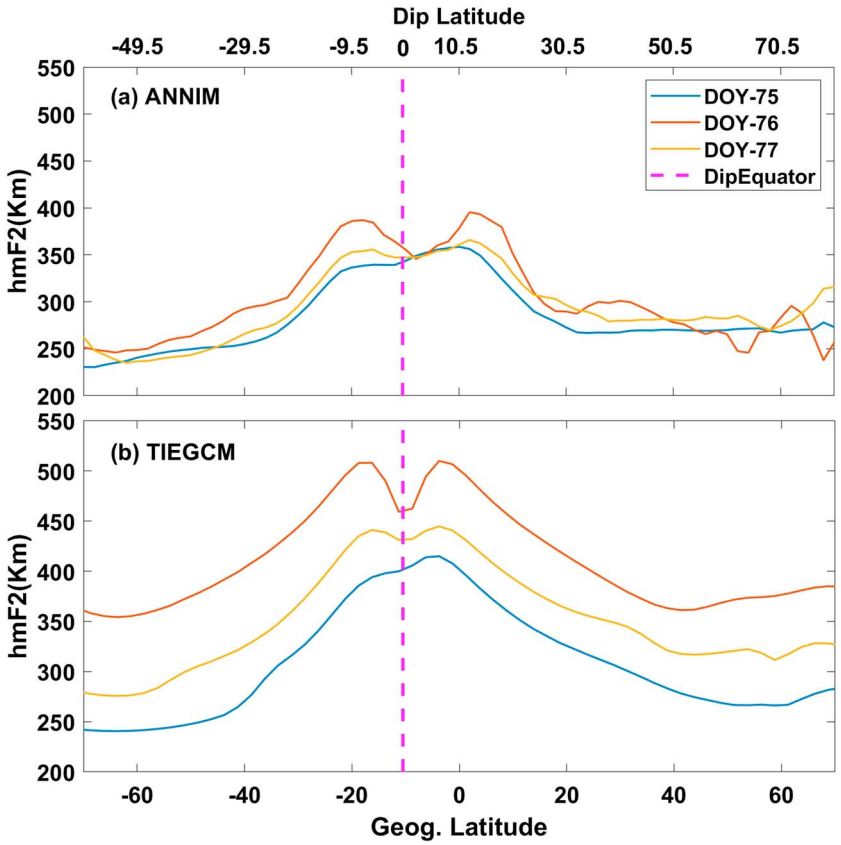

Figure 3. Latitudinal variation of h_mF_2 obtained from (a) artificial neural network-based ionospheric model (ANNIM) and (b) thermosphere-ionosphere-electrodynamics general circulation model (TIEGCM) around 90°W longitude at 16:30 UT. The vertical magenta line indicates the dip equator.

Figure 2 represents the local time and dip latitudinal variations of zonal mean N_mF_2 (Figures 2c and 2d) and h_mF_2 (Figures 2e and 2f) under quiet (DOY 75; 16 March 2015) and disturbed (DOY 76; 17 March 2015) geomagnetic conditions as predicted by ANNIM. Note that the F10.7 solar flux has increased around 35 sfu compared to the previous run of ANNIM (Figure 1). An overall enhancement in both N_mF_2 and h_mF_2 can be observed from Figure 2 due to the increased solar activity. The h_mF_2 around the equatorial and low-latitude regions is still showing the EHA structure (Figure 2e). However, the EHA is less significant compared to low solar activity (Figure 1b), which is consistent with the previous results by Luan et al. (2016). Further, it is evident from Figure 2e that the peak-to-trough difference predicted by ANNIM-2D reduced to ~10–15 km on Day 75, 2015. It is interesting to notice that the simulated EHA on storm day (Figure 2f) is more pronounced than the quiet time values (Figure 2e). Further, a large hemispheric asymmetry in EHA can be noticed from Figure 2f. The peak-to-trough differences of zonally averaged h_mF_2 are ~40 and 10 km in the Northern and Southern Hemispheres, respectively.

The vertical electron density distribution during the St. Patrick's Day storm is also explored to understand the variation of EHA and EIA. Since the ANNIM-2D is a two-dimensional model, we cannot get the altitudinal distribution of the electron density. Hence, we run the high-resolution version of the TIEGCM model to understand the general morphology of EHA during the geomagnetic storm. The F10.7 solar flux and 3-hourly Kp-index values are used as the TIEGCM input parameters. Though our study focused on Days 75–77, the model simulations were performed from Day 55. We focused our present study during the main phase of the storm where the IMF-B_z was steadily southward.

For better representation of the EHA, the latitudinal variation of h_mF_2 around 90°W longitude is plotted separately. For example, Figure 3 shows the latitudinal variation of h_mF_2 as predicted by (a) ANNIM-2D and (b) TIEGCM during the day numbers from 75 to 77. From Figures 3a and 3b, one can see that the

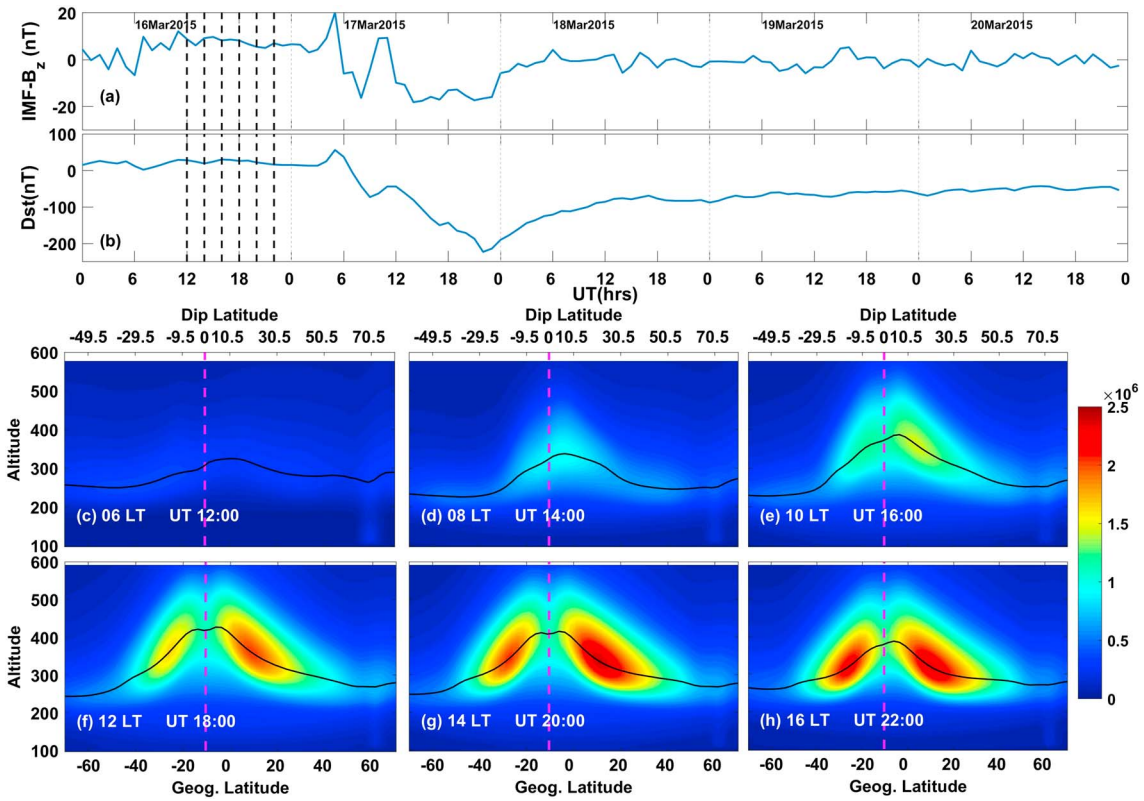

Figure 4. (a) IMF-Bz and (b) Dst index from Days 75 to 79 (16–20 March 2015). The latitudinal and altitudinal variation of electron density (c–f) over 90°W longitude as predicted by thermosphere-ionosphere-electrodynamics general circulation model on the day before the storm (day of the year 75; 16 March 2015). The vertical (black) dashed lines (left to right) in (a) and (b) represent the corresponding time of the electron density presented in plots (c)–(h). The black curve in each plot represents the h_mF_2 (c–h). The vertical magenta lines indicate the dip equator.

EHA is absent during the quiet time (DOY 75). The enhanced EHA can be observed on the storm day (DOY 76) in both ANNIM-2D and TIEGCM predicted h_mF_2 values. During the recovery phase of the storm (Day 77), we can still see the EHA, but it is less prominent compared to the storm day. The north-south averaged peak-to-trough difference is 42 km for ANNIM-2D and 50 km for TIEGCM, which are almost double that of the quiet time values.

With a view to examine the local time variation of observed EHA during the quiet and disturbed periods over the Brazilian longitude sector, the TIEGCM results over 90°W longitude sector are further analyzed. During the main phase of the storm (12:30 to 23 UT, 17 March 2015), Brazilian longitude (90±20°W) was in the morning to noon sector when the IMF-B_z was steadily southward; therefore, these longitudes are suitable to study the storm time variability of EHA. Figures 4a and 4b represent the IMF-B_z and Dst values, respectively, from Days 75 to 79 (16–20 March 2015). The latitudinal and altitudinal distribution of electron density at every 2-hr interval as predicted by TIEGCM on the day before the main phase (DOY 75; 16 March 2015) is presented in Figures 4c–4h. The vertical dashed lines (black) in Figures 4a and 4b (left to right) represent the corresponding time of the electron density presented in plots 4c–4h. The black curve in each plot represents the h_mF_2, and the vertical magenta line indicates the dip equator (Figures 4c–4h). It can be observed that the peak electron density and the height of maximum ionization located around the equatorial region during the early morning hours (Figures 4c and 4d). Around 10:00 LT, the ionization around the dip equator transported to low latitude due to the equatorial fountain process, leading to the formation of EIA. The plasma is further transported away from the dip equator due to the strong ExB, and a well-developed EIA can be seen around noon to afternoon hours. At 12:00–14:00 LT, one can see a double-peak structure around the low-latitude region; however, the peak-to-trough difference is less than 10 km. Further, it can be observed from Figure 4 that the EHA is less prominent during relatively high solar activity period, which is consistent with the previous study (Luan et al., 2016).

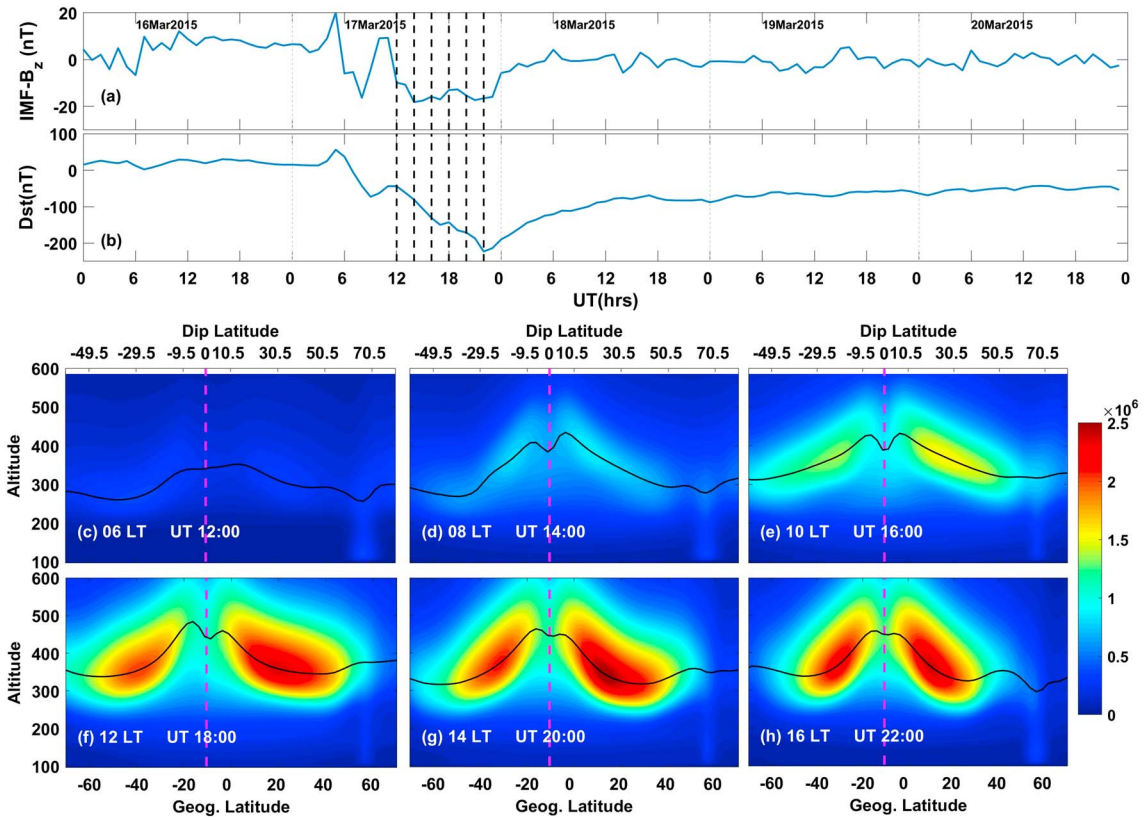

Figure 5. (a) IMF-Bz and (b) Dst index from Days 75 to 79 (16–20 March 2015). The latitudinal and altitudinal variation of electron density and the equatorial height anomaly (Figures 5c–5f) over 90°W longitude as predicted by thermosphere-ionosphere-electrodynamics general circulation model during the main phase of the St. Patrick's Day geomagnetic storm (day of the year 76; 17 March 2015). The vertical (black) dashed lines (left to right) in Figures 5a and 5b represent the corresponding time of the electron density presented in plots (c)–(h). The black curve in each plot represents the h_mF_2 (c–h). The vertical magenta lines indicate the dip equator.

Similarly, the vertical electron density distribution over 90°W longitude sector at every 2-hr interval is presented in Figures 5c–5h on DOY 76 (storm day). From Figure 5c, one can see that the ionospheric ceiling is located around the equatorial region during the early morning hours, similar to the DOY 75 (Figure 4c). However, around 8:00 LT (14:00 UT; Figure 5d), a clear double-peak structure in the h_mF_2 around ±10° dip latitude can be noticed during the main phase of the storm. The peak-to-trough difference is of ~50 km for the Northern Hemisphere and ~25 km for Southern Hemisphere at 8:00 LT. After 10 LT (Figure 5e), the EHA become nearly symmetric about the dip equator, and it is observed throughout the main phase of the storm. Further, a strong EHA can be noticed around 8:00–12:00 LT (Figures 5e–5h) with the averaged peak-to-trough differences varying from 30 to 55 km, which are significantly higher than the quiet time values. Another interesting observation from Figure 5d is that the occurrence of EHA during the main phase of the storm is almost 2 hr earlier than the usual time (Figure 1).

4. Discussion and Conclusions

The results presented in Figures 1 and 2 indicate that the ANNIM-2D could successfully reproduce the local time, latitude, and solar activity variations of EHA. Further, the EHA is more pronounced during the main phase of the storm compared to the quiet day (Figures 3–5). As discussed earlier, the vertical plasma drift and the diffusion along the magnetic field lines are the two key processes that control the plasma transport in the *F* layer. The equatorward wind can uplift the ionospheric plasma at the midlatitudes because of the inclined magnetic field lines. The nearly horizontal magnetic field lines at the equatorial and low-latitude regions make the meridional winds less effective; hence, the upward diffusion of plasma along the field lines is difficult to happen. However, the strong meridional winds can uplift the plasma at the low-latitude regions and

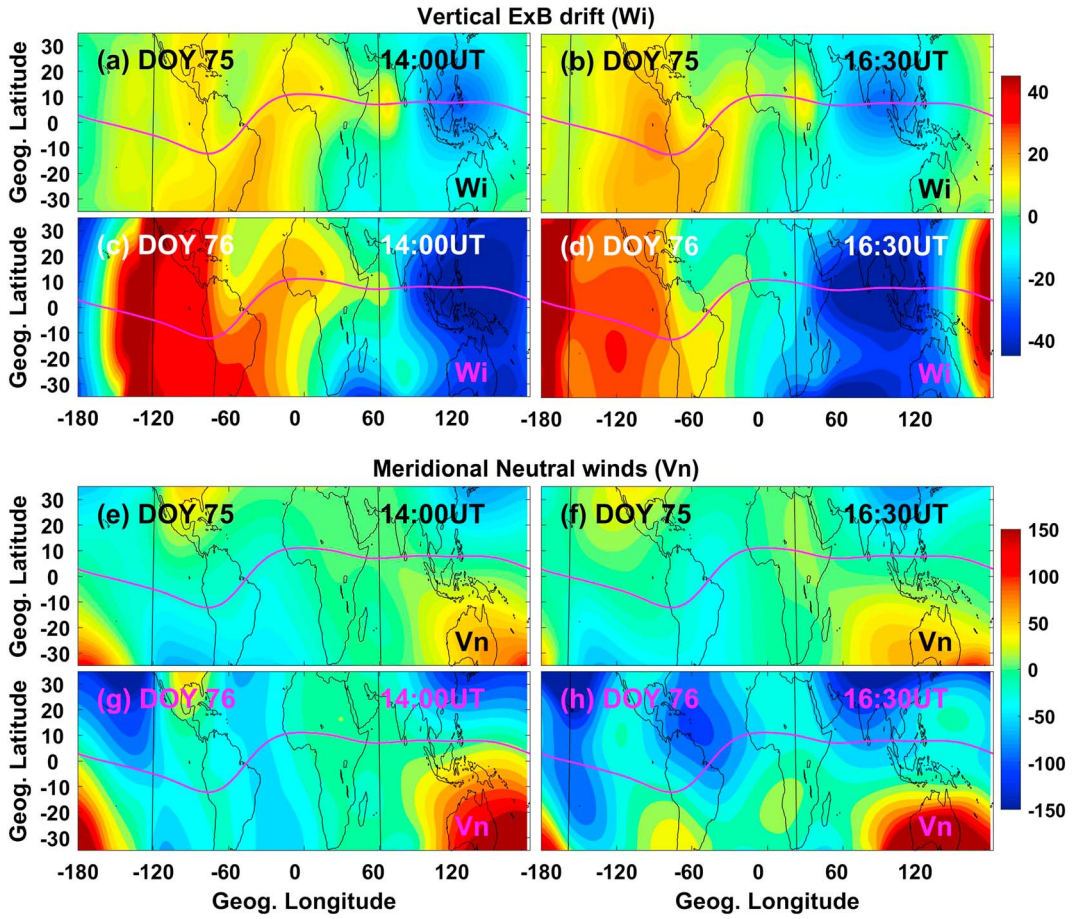

Figure 6. The vertical ExB plasma drift (+upward; a–d) and meridional neutral winds (+northward; e–g) at ~250-km altitude during quiet (DOY 75) and disturbed (DOY 76) periods as predicted by thermosphere-ionosphere-electrodynamics general circulation model. The magenta curves indicate dip equator. DOY = day of the year.

sometimes can transport the plasma to the opposite hemisphere. In general, the EPF is interpreted as the upward plasma drift at the equator and then followed by the downward diffusion along the magnetic field lines due to gravity and pressure gradient forces. If this is true, the ionospheric ceiling at 10:00 LT should locate at the equatorial region when the fountain is strong enough (Figure 1b). Recent studies showed that the vertical plasma drift and the diffusion are operating simultaneously over the equatorial region at all altitudes (Balan et al., 2017). The observed double-peak structure of the h_mF_2 during the low solar activity (Figure 1b) is due to field perpendicular ExB and the field-aligned diffusion of ionospheric electron density over the equatorial region, which operates at all heights. Besides the vertical plasma drift, the strength of meridional neutral winds and the solar ionization are also the contributing factors in the formation of EHA (Luan et al., 2016).

4.1. EHA During the Main Phase of the Storm

The EHA during the main phase of St. Patrick's Day storm is more pronounced than the quiet time as predicted by both ANNIM-2D and TIEGCM (Figures 2, 3, and 5). Further, it can be seen from Figures 4 and 5 that the formation of EHA during storm time is almost 2 hr earlier when compared to quiet time (Figure 5d). With a view to understand the responsible mechanisms for the enhanced EHA, the meridional neutral winds and vertical ExB plasma drifts are further analyzed during the quiet and disturbed time periods. For example, Figure 6 shows the vertical ExB plasma drifts (+upward; Figures 6a to 6d) and meridional neutral winds (+northward; Figures 6e to 6h) at ~250-km altitude during quiet (DOY 75) and disturbed (DOY 76) periods as predicted by TIEGCM at 14:00 UT (left panels) and 16:30 UT (right panels). From Figures 6a to 6d, one can clearly see that the vertical ExB drifts during the main phase of the geomagnetic

Table 1
Conditions Used in the Four Controlled Simulations

Model run	Parameters changed	Peak-to-trough difference (north-south averaged at 14:00 UT)	Peak-to-trough difference (north-south averaged at 16:30 UT)
0	Default	46 km	50 km
1	*Wi* = DOY 75; *Vn* = DOY 76	EHA is absent	19 km
2	*Wi* = DOY 76; *Vn* = DOY 75	43 km	53
3	*Wi* = DOY 75; *Vn* = DOY 75	EHA is absent	EHA is absent

Note. EHA = equatorial height anomaly; Wi = vertical EXB plasma drift; Vn = Meridional Neutral wind; DOY 75 represents the day before the storm (16 March 2015), and DOY 76 represents the main phase of the storm (17 March 2015).

storm (Figures 6c and 6d) are significantly enhanced compared to the quiet day (Figures 6a and 6b) over the longitude sectors between 120°W and 60°W. This could be due to the enhanced zonal electric field via PPEF (Hairston et al., 2016; Huang et al., 2016; Kalita et al., 2016; Kuai et al., 2016; Venkatesh et al., 2017; Zhang et al., 2017; Zhang et al., 2017; Zhou et al., 2016) during the main phase of the St. Patrick's Day storm. Further, Venkatesh et al. (2017) reported a strong PPEF over Brazilian sector during the main phase of the St. Patrick's Day storm. The enhancement of EHA observed in Figures 2, 3, and 5 could be due to the increased vertical plasma drifts associated with the PPEF during the main phase of storm. This intense plasma fountain (also referred as "super fountain") removed the electron density around the equatorial region and transport them to the low latitudes, which is causing the enhanced ionospheric height over ±10° dip latitudes during the main phase. Further, this intense plasma fountain is the main responsible factor for the early appearance of EHA in the morning longitude sector (Figure 5).

As the main phase of storm progresses, the particle precipitation at high latitudes causes joule heating, which can significantly alter the magnitude and direction of the meridional neutral winds. For example, Figures 6e to 6h show the meridional neutral winds (+Northward) at 14:00 UT (left panels) and 16:30 UT (right panels) as predicted by TIEGCM under quiet (DOY 75) and disturbed (DOY 76) geomagnetic conditions around 250-km altitude. The vertical black lines represent the solar terminator in each subplot. It can be observed from Figures 6e and 6f that during quiet time, the meridional wind circulations are from the equator to poleward on dayside, whereas the meridional winds blow toward the geographic equator on the nightside due to the differential heating of the Sun. In contrast to the quiet time wind circulation, a large meridional wind surge can be noticed during the storm day (Figures 6g and 6h) on the both dayside and nightside, which could be due to the Joule heating caused by enhanced particle precipitation at high latitudes (Blanc & Richmond, 1980; Fujiwara et al., 1996; Kuai et al., 2016; Lei et al., 2008; Tulasi Ram et al., 2010, 2015). The equatorward winds are strong enough to push the plasma along the magnetic field lines around ±10° latitude, which can enhance the EHA on the dayside during the main phase. The hemispheric asymmetry in the zonal mean EHA (Figure 2f) is probably due to the strong equatorward wind observed in the Northern Hemisphere during the storm time (Figure 6h) around these longitude sectors.

4.2. Relative Contribution of Vertical ExB Drifts and Meridional Neutral Winds

With a view to distinguish the relative importance of storm time meridional neutral winds and the vertical ExB plasma drifts, a series of case-controlled simulations are performed on the St. Patrick's day storm (DOY 76) using the TIEGCM model. An additional subroutine *new_oplus.F* is added to calculate the O^+ concentration in the controlled simulations without feedback to the main program. The conditions for each controlled simulation are described in Table 1. The vertical plasma drifts (*Wi*) and the meridional neutral winds (*Vn*) are replaced with the quiet time (DOY 75) values in the controlled simulations by following the method suggested by Ren and Lei (2017). Figure 7 shows the latitudinal and altitudinal distribution of the electron density around 90°W longitude sector at 14:00 UT (8:00 LT) obtained in the three controlled simulations on the storm day (DOY 76). The black curve in each subplot represents the h_mF_2. From Figure 7a, one can see the EHA around ±8° dip latitude region in the default run. The north-south averaged peak-to-trough difference is about 46 km. In the first controlled simulation (Run 1; Figure 7b), the storm time vertical ExB drifts

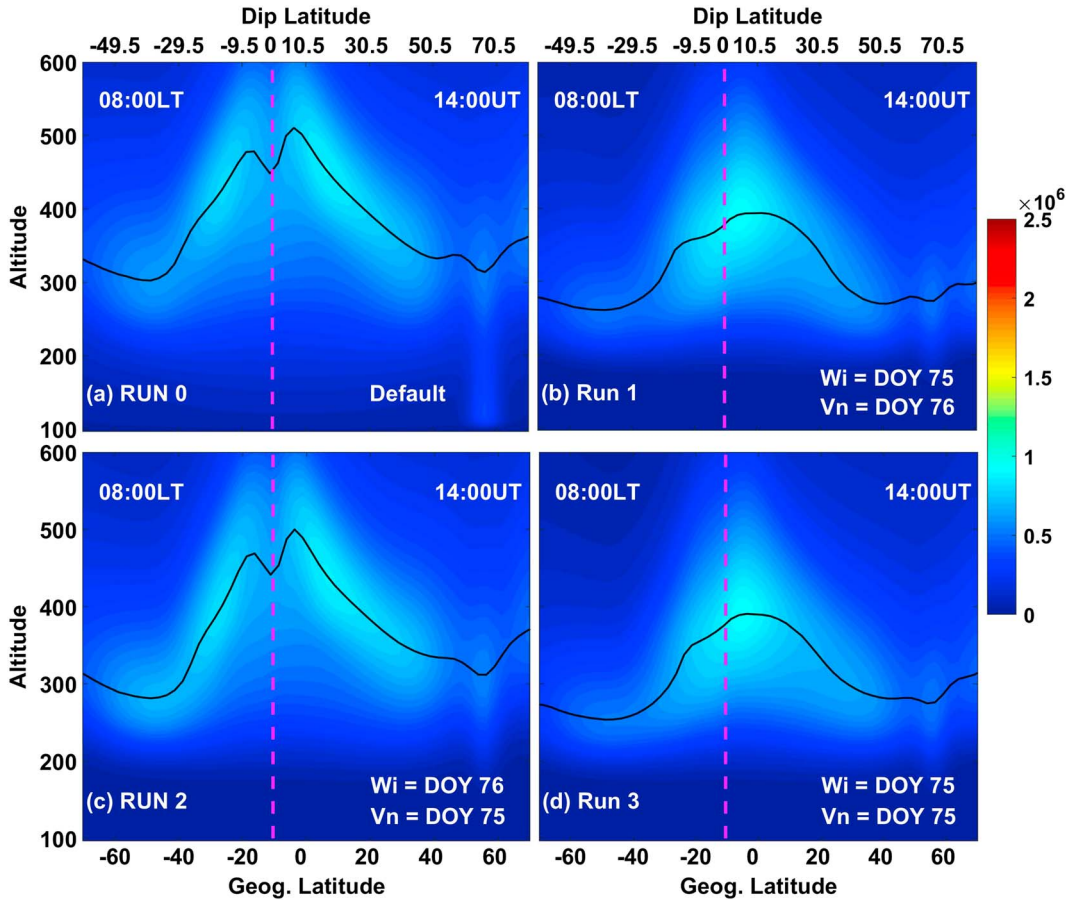

Figure 7. The latitudinal and altitudinal variation of the electron density around 90°W longitude sector at 14:00 UT obtained in the three controlled simulations (refer Table 1 for more details) on the storm day (DOY 76). *Wi* and *Vn* indicates the vertical ExB plasma drift and meridional neutral winds, respectively. The black curve in each subplot represents the h_mF_2. The vertical dashed lines indicate dip equator. DOY = day of the year.

are replaced with the previous quiet day (DOY 75) values, and the other parameters are unchanged. One can see that the EHA is completely disappeared in Run 1, which could be due the weaker equatorward winds at 14:00 UT during the storm time (Figure 6g). This indicates that the disturbance (equatorward) neutral winds alone cannot produce the EHA. In the second controlled simulation (Figure 7c), the meridional neutral winds are replaced with the quiet time values, and the storm time vertical ExB drifts are unchanged. Interestingly, the EHA in Figure 7c is still showing the pronounced h_mF_2 values around the low-latitude region, similar to the default run. The north-south-averaged peak-to-trough difference is around 43 km, which is similar to the default run. This indicates that the storm time-enhanced ExB drift significantly contributes to the development of EHA. In the final controlled simulation run, both meridional neutral winds and vertical ExB drifts are replaced with the quiet time values. One can notice from Figure 7d that the EHA is absent and the peak height is located around the equatorial region.

Similarly, the vertical electron density values obtained through the controlled simulations (similar to Figure 7) at 16:30 UT (10:30 LT) are also presented in Figure 8. From Figure 8a, one can see the pronounced EHA around ±10° dip latitude in the default run. The north-south averaged peak-to-trough difference is about 50 km. When the storm time vertical ExB drifts are replaced with the previous day (DOY 75) values and the other parameters are unchanged (Run 1), the EHA is significantly reduced in Run 1 compared to the default run (Figure 8b). The north-south-averaged peak-to-trough difference is ~19 km, which is much lesser than the default run. As shown in Figure 6h, one can notice the strong equatorward winds during the storm day as predicted by the TIEGCM simulations at 16:30 UT. Though the vertical plasma fountain is weaker in Run 1 (note that the quite time ExB drift is used in this run), strong meridional winds can

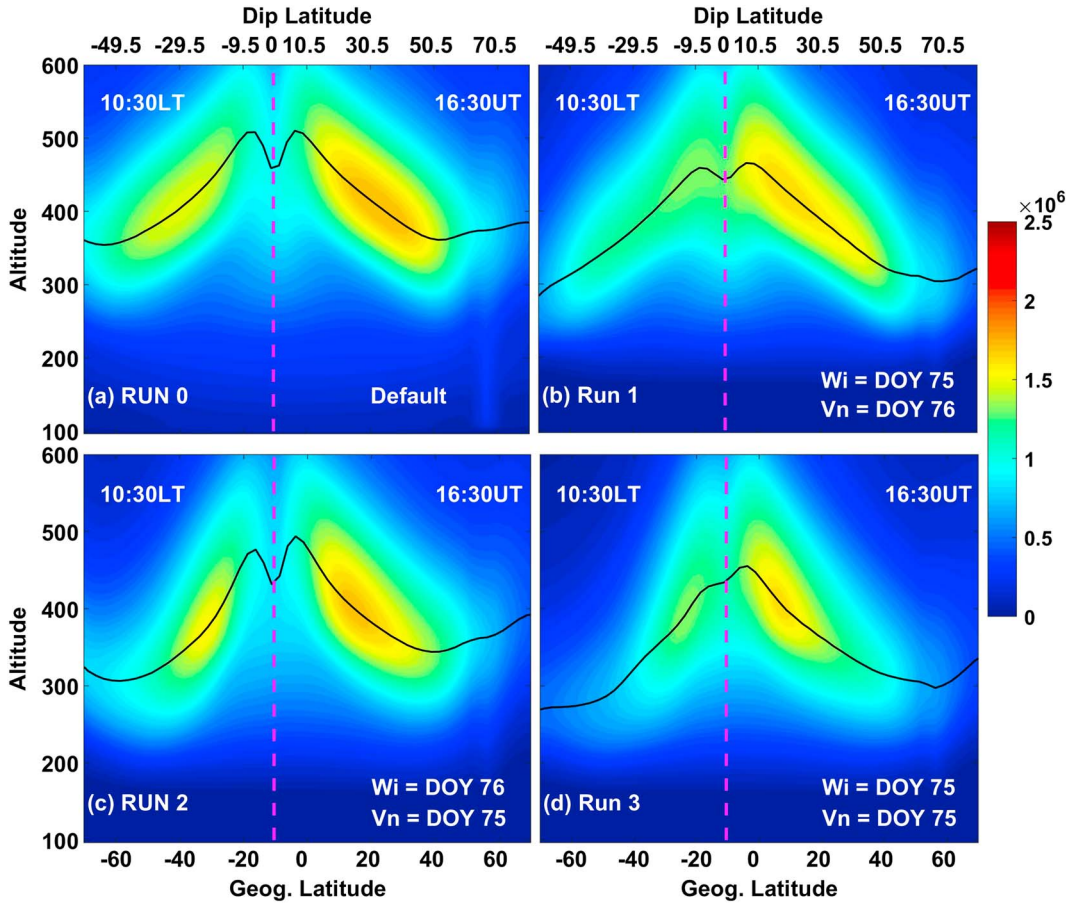

Figure 8. Same as Figure 7, but for 16:30 UT.

uplift the plasma at the low latitudes, leading to the formation of EHA. Since the transport due to winds is much weaker around low latitudes because of low inclination angles of field lines and the plasma fountain is weaker in this run, the magnitude of EHA is less significant compared to the default run (Run 0). In the second controlled simulation (Figure 8c), the meridional neutral winds are replaced with the quiet time values, and the storm time vertical ExB drifts are unchanged. Interestingly, the EHA in Figure 8c is still showing the pronounced h_mF_2 values around the low-latitude region, similar to the default run. The north-south-averaged peak-to-trough difference is around 55 km, which is significantly higher than Run 1 and more or less equal to Run 0. In the final controlled simulation run, one can notice that the EHA is completely disappeared and the ionospheric ceiling is located around the equatorial region when both meridional neutral winds and the vertical ExB are replaced with the quiet time values. Therefore, from the controlled simulation results presented in Figures 7 and 8, one can conclude that the enhanced vertical ExB plasma drift during main phase is the main responsible factor for the pronounced EHA (Figures 7c and 8c) although the enhanced equatorward neutral wind can positively contribute to the EHA (Figure 8b).

5. Summary

A detailed study is carried out on the EHA and its local time, latitude, and geomagnetic activity variations using the ANNIM-2D and TIEGCM during the main phase of St. Patrick's Day storm. The main results of the present work are summarized hereunder.

1. ANNIM-2D has successfully captured the spatial and temporal variability of the EHA during the low solar activity. The enhancement in the EHA is observed during the main phase of the storm in both ANNIM-2D and TIEGCM.

2. ANNIM-2D and TIEGCM show that the occurrence local time of EHA is much earlier (~2 hr) during the main phase of the geomagnetic storm compared to the quiet time.
3. TIEGCM control simulations revealed that the storm time enhancement of the equatorial fountain associated with the zonal electric field is the main responsible factor for the pronounced EHA.
4. The strong meridional neutral winds positively contribute to the enhancement of EHA under disturbed space weather conditions.

The enhancement in EHA during the main phase of the storm is mainly due to the immediate response of enhanced zonal electric field. Nevertheless, a detailed understanding about the EHA and its variability under varied solar and geomagnetic conditions are the topics that require more attention in future studies.

Acknowledgments
The work of V. Sai Gowtam was supported by the SCOSTEP Visiting Scholarship (SVS-2018) program. This work was supported by SERB, DST, Government of India through Project ECR-2017-002271. Xiaoli Luan was supported by the National Natural Science Foundation of China (41874184 and 41674154). Jiuhou Lei was supported by the National Natural Science Foundation of China (41831070 and 41325017), the Fundamental Research Funds for the Central Universities, and the Open Research Project of Large Research Infrastructures of CAS —"Study on the interaction between low/mid-latitude atmosphere and ionosphere based on the Chinese Meridian Project." The FORMOSAT-3/COSMIC-RO data were obtained from UCAR-CDAAC (http://cdaac-www.cosmic.ucar.edu/cdaac/products.html). The F10.7 solar flux and Kp-index were obtained from OMNIWEB, Goddard Space Flight Center web portal (http://omniweb.gsfc.nasa.gov/form/dx1.html). We sincerely acknowledge the National Center for Atmospheric Research (http://www.hao.ucar.edu/modeling/tgcm/) for providing the TIEGCM model codes. The simulated data can be accessed through Zenodo (https://zenodo.org/record/3270745#.XSGp8egzaUl).

References

Appleton, E. V. (1946). Two anomalies in the ionosphere. *Nature*, *157*(3995), 691. https://doi.org/10.1038/157691a0

Azpilicueta, F., & Brunini, C. (2011). A new concept regarding the cause of ionosphere semiannual and annual anomalies. *Journal of Geophysical Research*, *116*, A01307. https://doi.org/10.1029/2010JA015977

Balan, N., & Bailey, G. J. (1995). Equatorial plasma fountain and its effects—Possibility of an additional layer. *Journal of Geophysical Research*, *100*(A11), 21,421–21,432. https://doi.org/10.1029/95JA01555

Balan, N., Otsuka, Y., Bailey, G. J., Fukao, S., & Abdu, M. A. (2000). Annual variations of the ionosphere: A review based on the MU radar observations. *Advances in Space Research*, *25*(1), 153–162. https://doi.org/10.1016/S0273-1177(99)00913-8

Balan, N., Souza, J., & Bailey, G. J. (2017). Recent developments in the understanding of equatorial ionization anomaly: A review. *Journal of Atmospheric and Solar - Terrestrial Physics*, *171*, 3–11. https://doi.org/10.1016/j.jastp.2017.06.020

Bellchambers, W. H., & Piggott, W. R. (1958). Ionospheric measurements made at Halley Bay. *Nature*, *182*(4649), 1596–1597. https://doi.org/10.1038/1821596a0

Berkner, L. V., & Wells, H. W. (1938). Non-seasonal change of F2 region ion density. *Journal of Geophysical Research*, *43*(1), 15–36. https://doi.org/10.1029/TE043i001p00015

Blanc, M., & Richmond, A. D. (1980). The ionospheric disturbance dynamo. *Journal of Geophysical Research*, *85*(A4), 1669–1688. https://doi.org/10.1029/JA085iA04p01669

Bramley, E. N., & Peart, M. (1965). Effects of ionization transport on the equatorial F region. *Nature*, *206*(4990), 1245–1246. https://doi.org/10.1038/2061245a0

Burns, A. G., Solomon, S. C., Wang, W., Qian, L., Zhang, Y., Paxton, L. J., et al. (2015). Explaining solar cycle effects on composition as it relates to the winter anomaly. *Journal of Geophysical Research: Space Physics*, *120*, 5890–5898. https://doi.org/10.1002/2015JA021220

Burns, A. G., Wang, W., Qian, L., Solomon, S. C., Zhang, Y., Paxton, L. J., & Yue, X. (2014). On the solar cycle variation of the winter anomaly. *Journal of Geophysical Research: Space Physics*, *119*, 4938–4949. https://doi.org/10.1002/2013JA019552

Burns, A. G., Zeng, Z., Wang, W., Lei, J., Solomon, S. C., Richmond, A. D., et al. (2008). Behavior of the F2 peak ionosphere over the South Pacific at dusk during quiet summer condition from COSMIC data. *Journal of Geophysical Research*, *113*, A12305. https://doi.org/10.1029/2008JA013308

Chen, C. H., Huba, J. D., Saito, A., Lin, C. H., & Liu, J. Y. (2011). Theoretical study of the ionospheric Weddell Sea Anomaly using SAMI2. *Journal of Geophysical Research*, *116*, A04305. https://doi.org/10.1029/2010JA015573

Chen, Y., Liu, L., Le, H., Wan, W., & Zhang, H. (2016). Equatorial ionization anomaly in the low-latitude topside ionosphere: Local time evolution and longitudinal difference. *Journal of Geophysical Research: Space Physics*, *121*, 7166–7182. https://doi.org/10.1002/2016JA022394

Dang, T., Wang, W., Burns, A., Dou, X., Wan, W., & Lei, J. (2017). Simulations of the ionospheric annual asymmetry: Sun-Earth distance effect. *Journal of Geophysical Research: Space Physics*, *122*, 6727–6736. https://doi.org/10.1002/2017JA024188

Dudeney, J. R., & Piggott, W. R. (1978). Antarctic ionospheric research. In L. J. Lanzerotti & C. G. Park (Eds.), *Upper Atmosphere Research in Antarctica. Ant. Res. Ser* (pp. 200–235). Washington, DC: American Geophysical Union. https://doi.org/10.1029/AR029p0200

Fujiwara, H., Maeda, S., Fukunishi, H., Fuller-Rowell, T., & Evans, D. S. (1996). Global variations of thermospheric winds and temperatures caused by substorm energy injection. *Journal of Geophysical Research*, *101*(A1), 225–239. https://doi.org/10.1029/95JA01157

Gulyaeva, T. L., Bradley, P. A., Stanislawska, I., & Juchnikowski, G. (2008). Towards a new reference model of hmF2 for IRI. *Advances in Space Research*, *42*(4), 666–672. https://doi.org/10.1016/j.asr.2008.02.021

Hairston, M., Coley, W. R., & Stoneback, R. (2016). Responses in the polar and equatorial ionosphere to the March 2015 St. Patrick Day storm. *Journal of Geophysical Research: Space Physics*, *121*, 11,213–11,234. https://doi.org/10.1002/2016JA023165

He, M., Liu, L., Wan, W., Ning, B., Zhao, B., Wen, J., et al. (2009). A study of the Weddell Sea Anomaly observed by FORMOSAT-3/COSMIC. *Journal of Geophysical Research*, *114*, A12309. https://doi.org/10.1029/2009JA014175

Heelis, R. A., Lowell, J. K., & Spiro, R. W. (1982). A model of the high-latitude ionospheric convection pattern. *Journal of Geophysical Research*, *87*(6339), 1982.

Hoque, M. M., & Jakowski, N. (2012). A new global model for the ionospheric F2 peak height for radio wave propagation. *Annals of Geophysics*, *30*(5), 797–809. https://doi.org/10.5194/angeo-30-797-2012

Huang, C. S., Foster, J. C., & Kelley, M. C. (2005). Long-duration penetration of the planetary electric field to the low-altitude ionosphere during the main phase of magnetic storms. *Journal of Geophysical Research*, *110*, A11309. https://doi.org/10.1029/2005JA011202

Huang, C. S., Sazykin, S., Chau, J. L., Maruyama, N., & Kelley, M. C. (2007). Penetration electric fields: Efficiency and characteristic time scale. *Journal of Atmospheric and Solar-Terrestrial Physics*, *69*(10-11), 1135–1146. https://doi.org/10.1016/j.jastp.2006.08.016

Huang, C.-S., Wilson, G. R., Hairston, M. R., Zhang, Y., Wang, W., & Liu, J. (2016). Equatorial ionospheric plasma drifts and O^+ concentration enhancements associated with disturbance dynamo during the 2015 St. Patrick's Day magnetic storm. *Journal of Geophysical Research: Space Physics*, *121*, 7961–7973. https://doi.org/10.1002/2016JA023072

Jee, G., Burns, A. G., Kim, Y. -H., & Wang, W. (2009). Seasonal and solar activity variations of the Weddell Sea Anomaly observed in the TOPEX total electron content measurements. *Journal of Geophysical Research*, *114*, A04307. https://doi.org/10.1029/2008JA013801

Kalita, B. R., Hazarika, R., Kakoti, G., Bhuyan, P. K., Chakrabarty, D., Seemala, G. K., et al. (2016). Conjugate hemisphere ionospheric response to the St. Patrick's Day storms of 2013 and 2015 in the 100°E longitude sector. *Journal of Geophysical Research: Space Physics*, *121*, 11,364–11,390. https://doi.org/10.1002/2016JA023119

Kikuchi, T., & Hashimoto, K. (2016). Transmission of the electric fields to the low latitude ionosphere in the magnetosphere-ionosphere current circuit. *Geoscience Letters*, *3*(1). https://doi.org/10.1186/s40562-016-0035-6

Kikuchi, T., Hashimoto, K., & Nozaki, K. (2008). Penetration of magnetospheric electric fields to the equator during a geomagnetic storm. *Journal of Geophysical Research*, *113*, A06214. https://doi.org/10.1029/2007JA012628

Kikuchi, T., Luhr, H., Schlegel, K., Tachihara, H., Shinohara, M., & Kitamura, T. L. (2000). Penetration of auroral electric fields to the equator during a substorm. *Journal of Geophysical Research*, *105*(A10), 23,251–23,261. https://doi.org/10.1029/2000JA900016

Kuai, J., Liu, L., Liu, J., Sripathi, S., Zhao, B., Chen, Y., et al. (2016). Effects of disturbed electric fields in the low-latitude and equatorial ionosphere during the 2015 St. Patrick's Day storm. *Journal of Geophysical Research: Space Physics*, *121*, 9111–9126. https://doi.org/10.1002/2016JA022832

Lei, J., Wang, W., Burns, A. G., Solomon, S. C., Richmond, A. D., Wiltberger, M., et al. (2008). Observations and simulations of the ionospheric and thermospheric response to the December 2006 geomagnetic storm: Initial phase. *Journal of Geophysical Research*, *113*, A01314. https://doi.org/10.1029/2007JA012807

Lin, C. H., Liu, J. Y., Cheng, C. Z., Chen, C. H., Liu, C. H., Wang, W., et al. (2009). Three dimensional ionospheric electron density structure of the Weddell Sea Anomaly. *Journal of Geophysical Research*, *114*, A02312. https://doi.org/10.1029/2008JA013455

Liu, H., Thampi, S. V., & Yamamoto, M. (2010). Phase reversal of the diurnal cycle in the midlatitude ionosphere. *Journal of Geophysical Research*, *115*, A01305. https://doi.org/10.1029/2009JA014689

Lu, G., Goncharenko, L. P., Nicolls, M. J., Maute, A. I., Coster, A. J., & Paxton, L. J. (2012). Ionospheric and thermospheric variations associated with prompt penetration electric fields. *Journal of Geophysical Research*, *117*, A08312. https://doi.org/10.1029/2012JA017769

Luan, X., Lei, J., Dou, X., & Dang, T. (2016). Double crests of peak height in the equatorial ionospheric F2 layer observed by COSMIC. *Journal of Geophysical Research: Space Physics*, *121*, 529–537. https://doi.org/10.1002/2015JA021611

Ma, R., Xu, J., & Liao, H. (2003). The features and a possible mechanism of semiannual variation in the peak electron density of the low latitude F2 layer. *Journal of Atmospheric and Solar-Terrestrial Physics*, *65*(1), 47–57. https://doi.org/10.1016/S1364-6826(02)00192-X

Maruyama, T., Uemoto, J., Ishii, M., Tsugawa, T., Supnithi, P., & Komolmis, T. (2014). Low-latitude ionospheric height variation as observed by meridional ionosonde chain: Formation of ionospheric ceiling over the magnetic equator. *Journal of Geophysical Research: Space Physics*, *119*, 10,595–10,607. https://doi.org/10.1002/2014JA020215

Mendillo, M., Huang, C.-L., Pi, X., Rishbeth, H., & Meier, R. (2005). The global ionospheric asymmetry in total electron content. *Journal of Atmospheric and Solar-Terrestrial Physics*, *67*(15), 1377–1387. https://doi.org/10.1016/j.jastp.2005.06.021

Millward, G. H., Rishbeth, H., Fuller-Rowell, T. J., Aylward, A. D., Quegan, S., & Moffett, R. J. (1996). Ionospheric F2 layer seasonal and semiannual variation. *Journal of Geophysical Research*, *101*(A3), 5149–5156. https://doi.org/10.1029/95JA03343

Moffett, R. J., & Hanson, W. B. (1965). Effect of ionization transport on the equatorial *F* region. *Nature*, *206*(4985), 705–706. https://doi.org/10.1038/206705a0

Nishida, A. (1968). Coherence of geomagnetic DP 2 fluctuations with interplanetary magnetic variations. *Journal of Geophysical Research*, *73*(17), 5549–5559. https://doi.org/10.1029/JA073i017p05549

Pavlov, A. V., & Pavlova, N. M. (2009). Anomalous variations of NmF2 over the Argentine Islands: A statistical study. *Annals of Geophysics*, *17*, 794–805.

Penndorf, R. (1965). The average ionospheric conditions over the Antarctic. In A. H. Waynick (Ed.), *Geomagnetism and Aeronomy. Ant. Res. Ser* (Vol. 4, pp. 1–45). Washington, DC: American Geophysical Union.

Ren, D., & Lei, J. (2017). A simulation study of the equatorial ionospheric response to the October 2013 geomagnetic storm. *Journal of Geophysical Research: Space Physics*, *122*, 9696–9704. https://doi.org/10.1002/2017JA024286

Richmond, A. D., Ridley, E. C., & Roble, R. G. (1992). A thermosphere/ionosphere general circulation model with coupled electrodynamics. *Geophysical Research Letters*, *6*, 601–604.

Rishbeth, H., & Garriott, O. K. (1969). *Introduction to ionospheric physics* (pp. 1–202). New York and London: Academic Press.

Rishbeth, H., & Muller-Wodarg, I. C. F. (2006). Why is there more ionosphere in January than in July? The annual asymmetry in the F2-layer. *Annals of Geophysics*, *24*(12), 3293–3311. https://doi.org/10.5194/angeo-24-3293-2006

Rishbeth, H., & Setty, C. S. G. K. (1961). The F-layer at sunrise. *Journal of Atmospheric and Terrestrial Physics*, *21*, 263–276.

Sai Gowtam, V., & Tulasi Ram, S. (2017a). An artificial neural network based ionospheric model to predict N_mF_2 and h_mF_2 using long-term data set of FORMOSAT-3/COSMIC radio occultation observations: Preliminary results. *Journal of Geophysical Research: Space Physics*, *122*, 11,743–11,755. https://doi.org/10.1002/2017JA024795

Sai Gowtam, V., & Tulasi Ram, S. (2017b). Ionospheric annual anomaly—New insights to the physical mechanisms. *Journal of Geophysical Research: Space Physics*, *122*, 8816–8830. https://doi.org/10.1002/2017JA024170

Sai Gowtam, V., & Tulasi Ram, S. (2017c). Ionospheric winter anomaly and annual anomaly observed from Formosat-3/COSMIC radio occultation observations during the ascending phase of solar cycle 24. *Advances in Space Research*, *60*(8), 1585–1593. https://doi.org/10.1016/j.asr.2017.03.017

Torr, M. R., & Torr, D. G. (1973). The seasonal behaviour of the F2-layer of the ionosphere. *Journal of Atmospheric and Solar-Terrestrial Physics*, *35*(12), 2237–2251. https://doi.org/10.1016/0021-9169(73)90140-2

Tulasi Ram, S., Liu, C. H., & Su, S.-Y. (2010). Periodic solar wind forcing due to recurrent coronal holes during 1996–2009 and its impact on Earth's geomagnetic and ionospheric properties during the extreme solar minimum. *Journal of Geophysical Research*, *115*, A12340. https://doi.org/10.1029/2010JA015800

Tulasi Ram, S., Sai Gowtam, V., Mitra, A., & Reinisch, B. (2018). The improved two-dimensional artificial neural network-based ionospheric model (ANNIM). *Journal of Geophysical Research: Space Physics*, *123*, 5807–5820. https://doi.org/10.1029/2018JA025559

Tulasi Ram, S., Yokoyama, T., Otsuka, Y., Shiokawa, K., Sripathi, S., Veenadhari, B., et al. (2015). Duskside enhancement of equatorial zonal electric field response to convection electric fields during the St. Patrick's Day storm on 17 March 2015. *Journal of Geophysical Research: Space Physics*, *121*, 538–548. https://doi.org/10.1002/2015JA021932

Venkatesh, K., Tulasi Ram, S., Fagundes, P. R., Seemala, G. K., & Batista, I. S. (2017). Electrodynamic disturbances in the Brazilian equatorial and low-latitude ionosphere on St. Patrick's Day storm of 17 March 2015. *Journal of Geophysical Research: Space Physics*, *122*, 4553–4570. https://doi.org/10.1002/2017JA024009

Volland, H. (1969). The upper atmosphere as a multiple refractive medium for neutral air motions. *Journal of Atmospheric and Solar-Terrestrial Physics*, *31*(4), 491–514. https://doi.org/10.1016/0021-9169(69)90002-6

Yonezawa, T. (1971). The solar-activity and latitudinal characteristics of the seasonal, non-seasonal and semi-annual variations in the peak electron densities of the F2-layer at noon and at midnight in middle and low latitudes. *Journal of Atmospheric and Solar-Terrestrial Physics*, *33*, 887–907.

Yonezawa, T., & Arima, Y. (1959). On the seasonal and non-seasonal annual variations and the semi-annual variation in the noon and midnight electron densities of the F2 layer in middle latitudes. *Journal Radio Research Labs*, *6*, 293–309.

Zeng, Z., Burns, A., Wang, W., Lei, J., Solomon, S., Syndergaard, S., et al. (2008). Ionospheric annual asymmetry observed by the COSMIC radio occultation measurements and simulated by the TIEGCM. *Journal of Geophysical Research*, *113*, A07305. https://doi.org/10.1029/2007JA012897

Zhang, M.-L., Liu, L., Wan, W., & Ning, B. (2014). An update global model of h_mF_2 from values estimated from ionosonde and COSMIC/FORMOSAT-3 radio occultation. *Advances in Space Research*, *53*(3), 395–402. https://doi.org/10.1016/j.asr.2013.11.053

Zhang, S.-R., Erickson, P. J., Zhang, Y., Wang, W., Huang, C., Coster, A. J., et al. (2017). Observations of ion-neutral coupling associated with strong electrodynamic disturbances during the 2015 St. Patrick's Day storm. *Journal of Geophysical Research: Space Physics*, *122*, 1314–1337. https://doi.org/10.1002/2016JA023307

Zhang, S.-R., Zhang, Y., Wang, W., & Verkhoglyadova, O. P. (2017). Geospace system responses to the St. Patrick's Day storms in 2013 and 2015. *Journal of Geophysical Research: Space Physics*, *122*, 6901–6906. https://doi.org/10.1002/2017JA024232

Zhou, Y.-L., Lühr, H., Xiong, C., & Pfaff, R. F. (2016). Ionospheric storm effects and equatorial plasma irregularities during the 17–18 March 2015 event. *Journal of Geophysical Research: Space Physics*, *121*, 9146–9163. https://doi.org/10.1002/2016JA023122